Analysis of particulate composite behaviour based on non-linear elasticity and modulus degradation theory

F. C. WONG*, A. AIT-KADI
CERSIM, Department of Chemical Engineering, Laval University Quebec, Quebec, Canada G1K 7P4

A micromechanical model for the analysis of particulate mechanical behaviour is presented. Non-linear effects were introduced in the model by a non-linear elastic description of the matrix and through a modulus degradation routine. The first part of the study used the experimental data from a range of glass bead/HTPB composites to back-calculate model parameters. The results showed that the model gave a good representation of the processes believed to control mechanical behaviour. These processes include partial particle debonding and progressive debonding from the largest to smallest particles throughout the strain history. The second part of the study examined the sensitivity of the model results to small changes in the adjustable input parameters. The residual bond in a debonded particle was found to have a dominating effect on the calculated results. Based on the sensitivity results, "best guess" interaction and debonding parameters were selected to examine the predictive capability of the model. In most cases, the predicted composite stresses were within 10% of the experimental data. Dilatation was usually over-predicted. The results showed that the model was capable of predicting the mechanical behaviour as long as suitable values for critical stress and adhesion energy were available.

Nomenclature

$L \equiv$ length $F \equiv$ force $T \equiv$ time; square brackets [ ] denote dimensions of the quantity

A	debonded surface area of inclusion, $[L^2]$
A_{ijkl}	$(C^{i}_{ijmn} - C^{o}_{ijmn})^{-1} C^{o}_{mnkl}$, $[FL^{-2}]$
a_i	fitting coefficients for matrix polynomial
B_{ijkl}	$(C^{v}_{ijmn} - C^{o}_{ijmn})^{-1} C^{o}_{mnkl}$, $[FL^{-2}]$
C_{ijkl}	average elastic constants of composite, $[FL^{-2}]$
C^{o}_{ijkl}	elastic constants of comparison material, $[FL^{-2}]$
C^{r}_{ijkl}	elastic constants of phase r material, $[FL^{-2}]$
c^{i}	volume fraction of inclusions
c^{i}_{o}	initial volume fraction of inclusions
c^{r}	volume fraction of phase-r inclusion
c^{v}	volume fraction of voids or vacuoles
$d\varepsilon_{area}$	energy dissipated through surface creation, $[FL]$
$d\varepsilon_{mod}$	net internal strain energy due to modulus degradation, $[FL]$
E_c	average composite tensile modulus, $[FL^{-2}]$
E_i	inclusion tensile modulus, $[FL^{-2}]$
E_{ij}	tensile modulus in ij direction, $[FL^{-2}]$
E_o	matrix tensile modulus, $[FL^{-2}]$
E^{r}_{o}	reference stress relaxation modulus at $t = 1$, $[FL^{-2}]$
$E(t)$	stress relaxation modulus, $[FL^{-2}]$
F_b	partial debonding factor
F^{err}_{b}	average absolute error for finding F_b,
G_c	adhesion energy, $[FL]$
G^{app}_{c}	apparent adhesion energy, $[FL]$
G_o	matrix shear modulus, $[FL^{-2}]$
I_{ijkl}	identity matrix
K_o	matrix bulk modulus, $[FL^{-2}]$
M_ε	composite strain magnification factor
m	exponent in stress relaxation power law
n	log standard deviation in particle distribution
r	particle radius, $[L]$
$\bar{r}$	mean particle radius, $[L]$
S^{r}_{ijkl}	Eshelby matrix of phase r material
t	time, $[T]$
dV/V	composite volume dilatation
V_o	specimen volume, $[L^3]$
Y	interaction function
Y_m	interaction function multiplier
Y^{err}_{m}	average relative error for finding Y_m
ε_{cr}	critical strain, $[L/L]$
ε_{ij}	average composite strain in ij direction $[L/L]$

*Also: Defence Research Establishment Valcartier, Val Belair, Quebec, Canada, G3J 1X5; to which all correspondence should be addressed.

0022–2461

ε_c	average composite uniaxial strain, $[L/L]$
ε_o	average uniaxial matrix strain, $[L/L]$
Γ^r_{ijkl}	correction matrix of phase r material
ν_{ij}	Poisson ratio in ij direction
ν_o	matrix Poisson's ratio
σ_{cr}	critical stress, $[FL^{-2}]$
σ_{ij}	composite stress in ij direction, $[FL^{-2}]$
σ_c^{eng}	average composite engineering stress, $[FL^{-2}]$
σ_c^T	average composite true stress, $[FL^{-2}]$

1. Introduction

The prediction of solid-propellant mechanical behaviour has attracted the attention of many researchers over the years [1–11]. During that time, much of the effort was concentrated on the development of phenomenological models that treated propellant as a homogeneous material. Other researchers took a different approach and treated propellant as a particulate composite [12–17]. The micromechanical analyses carried out by these researchers provided insight to the physical processes that controlled particulate composite or propellant behaviour.

It was recognized early on that volume change was closely linked to the non-linear behaviour which a particulate composite exhibited as it was loaded. Smith [18] and Farris [19], hypothesized that particulate composites exhibited three distinct regions in their stress–strain behaviour. The initial region was controlled primarily by the initial inclusion concentration and the matrix properties. A transition region delimited the beginning and completion of inclusion debonding. Application of strain in the last region was believed only to stretch the binder and enlarge existing vacuoles. A vacuole was defined as a spheroidal air pocket which entrapped a debonded inclusion.

A different hypothesis on inclusion debonding was advanced by Vratsanos–Anderson and Farris [20, 21]. Here the authors assumed that inclusion debonding was continuous throughout the strain history. Constituents were assumed to be linear elastic. Their micromechanical model parameterized several experimentally observed phenomena such as the relationships between reinforcement and particle size [22–25], reinforcement and adhesion [26–29] and inclusion concentration and modulus [30, 31] in a computationally tractable manner. In the range of analysis techniques covering semi-empirical formulations [32, 33], variational formulations [34–36] and approximate methods [37–40], their model fell in the approximate category because debonding at a microscopic level was quantified by modulus prediction routines that calculated average composite properties.

An evaluation of the combined concentration decrease/void addition model by Vratsanos–Anderson and Farris [20, 21] was made by Wong and Ait-Kadi [41] using a glass bead/polyethylene composite. The model decreased the inclusion concentration because inclusions were debonded, and replaced them by equivalent-sized voids. A void was defined as a spherical air pocket with isotropic properties. Following Vratsanos–Anderson and Farris [20, 21], the linear elastic constituent assumption was retained. It was concluded that the model could predict the mechanical behaviour of highly loaded composites if a representative adhesion energy was available and if matrix non-linearity was accounted for.

The model used previously [41] was improved [42] by implementing a modulus prediction routine based on the Mori–Tanaka (M–T) method [43] and the work of Ju and Chen [44]. The addition of Ju and Chen's modulus correction matrix to the M–T method accounted for additional reinforcing effects due to particle interaction. The improved M–T routine allowed debonded inclusions to be modelled as vacuoles by attributing orthotropic elastic constants to them.

The merits of the improved M–T routine were evaluated using literature data. Results showed that at high inclusion volume fractions, correct modulus predictions could only be made by accounting for particle interaction effects. Comparison of the new micromechanical model based on the improved M–T method with experimental data showed that modelling debonded particles by vacuoles instead of voids gave more representative results. The performance of the new model was limited, like the original model, by the assumed linear elastic matrix.

In this paper, the implementation of a routine in the M–T based micromechanical model to account for a non-linear elastic matrix is described. The validity of the assumptions on which the model is based is then explored. This shows that the assumption of continuous inclusion debonding throughout the strain history is justifiable. A comparison of calculated and experimentally measured parameters that are believed to control composite behaviour is made using the results from a glass bead/polybutadiene composite system. Finally, a sensitivity analysis shows that the micromechanical model can produce accurate results, as long as representative adhesive characteristics are available.

2. Non-linear elastic micromechanical model

This section will outline the equations that define the non-linear elastic micromechanical model. The development will begin with a statement of the governing energy equation and then move to a description of improved M–T modulus prediction routine. The implementation of the non-linear matrix properties will then be discussed.

2.1. Governing energy equation

For any deformable material, the state of stress and strain in a structure can be calculated for a system of loads or displacements using the first law of thermodynamics. In the case of particulate composites, external work is not only stored as internal strain energy but is dissipated through the process of particle debonding. It was shown [20, 41], that this statement could be expressed as

$$2G_c\delta A/V_o = \sigma_{ij}\delta\varepsilon_{ij} - \delta\sigma_{ij}\varepsilon_{ij} \quad (1)$$

where G_c is the adhesion energy between particle and matrix, δA is the variation or creation of surface area through debonding, σ_{ij} is the composite stress, ε_{ij} is the composite strain and V_o is the specimen volume.

By using the boundary conditions for a uniaxial bar under tension (1 1-direction) and ambient pressure, the constitutive equation for an orthotropic material can be shown to be [42]

$$\sigma_{11} = \left(\bar{C}_{1111} - \frac{2\bar{C}_{1122}\bar{C}_{2211}}{\bar{C}_{2222} + \bar{C}_{2233}}\right)\varepsilon_{cr} \quad (2)$$

where σ_{11} is the true stress in the loading direction and ε_{cr} the uniaxial critical strain. Critical strain is defined to be the point where the internal strain energy in the composite and the energy dissipated through particle debonding equals the work put into the composite. In this article, all stress measures are in terms of true stress, while strains are defined in terms of engineering strain. This distinction is particularly important when comparisons are made between model results and experimental data in Section 4.1. It can be seen from Equation 2 that the average composite tensile modulus, E_c, is defined by

$$E_c = \bar{C}_{1111} - \frac{2\bar{C}_{1122}\bar{C}_{2211}}{\bar{C}_{2222} + \bar{C}_{2233}} \quad (3)$$

By differentiating σ_{11} with respect to the bonded particle concentration, c_i, and substituting it and Equation 2 into Equation 1 gives

$$\begin{aligned} 2\frac{G_c}{V_o}\frac{dA}{dc_i} = \Bigg[& -\frac{d}{dc_i}\bar{C}_{1111} - 2\frac{\bar{C}_{1122}\bar{C}_{2211}}{(\bar{C}_{2222} + \bar{C}_{2233})^2} \\ & \times\left(\frac{d}{dc_i}\bar{C}_{2222} + \frac{d}{dc_i}\bar{C}_{2233}\right) \\ & + 2\frac{\bar{C}_{2222} + \bar{C}_{2233}}{(\bar{C}_{2222} + \bar{C}_{2233})^2} \\ & \times\left(\bar{C}_{2211}\frac{d}{dc_i}\bar{C}_{1122} + \bar{C}_{1122}\frac{d}{dc_i}\bar{C}_{2211}\right)\Bigg]\varepsilon_{cr}^2 \end{aligned} \quad (4)$$

This equation assumes that the representative volume element (RVE) is larger than the largest particle, so that average stress, strain and moduli can be used. Equation 4 can also be summarized by

$$d\varepsilon_{area} = d\varepsilon_{mod} \quad (5)$$

where $d\varepsilon_{area}$ is the energy dissipated through surface creation and is equal to the left-hand side of Equation 4 and $d\varepsilon_{mod}$ is the net internal strain energy due to modulus degradation and is equal to the right-hand side of Equation 4.

2.2. Relationship between surface area and inclusion concentration

The relationship between increase in surface area due to a decrease in bonded particle concentration can be shown to be [45]

$$\frac{dA}{dc_i} = -2\frac{3(1 - \sin\theta)}{r}V_o \quad (6)$$

where r is the particle radius. The factor 2 in Equation 6 accounts for the fact that when a particle debonds, two new surfaces are created. The $\sin\theta$ term has been included to leave open the possibility that a particle may partially debond θ° from the equator up to the pole. When $\theta = 0^\circ$, dA/dc_i reaches a maximum of $-6V_o/r$.

The types of particles used for this study were characterized with a log normal size distribution [41] defined by

$$\log r = \log\bar{r} + n \quad (7)$$

where r is the particle radius, $\bar{r}$ is the mean particle radius and n is the log standard deviation.

2.3. Elastic properties of a three-phase composite

Equation 4 requires that a relationship between the volume fraction of the constituent phases and the average composite modulus be known. Initially, a particulate composite can be essentially considered as a material containing only two distinct phases as long as the initial void fraction is negligible. However, at some critical stress level, σ_{cr}, enough energy is input into the material system so that particles begin to debond. According to Equations 4 and 6, the larger the particle, the lower the energy required for it to debond. When debonding occurs, the composite changes from a two-phase composite containing well-bonded particles and a matrix to a three-phase composite containing well-bonded particles, debonded particles and a matrix. Modelling debonded particles by a vacuole representation gives rise to orthotropic composite properties because the stiffness in the direction of loading is lower than the stiffness perpendicular to the load.

The average elastic properties for a three-phase composite $[\bar{C}]$ containing well-bonded particles with properties $[C^i]$, matrix with properties $[C^o]$ and vacuoles with properties $[C^v]$ was derived [42] to be

$$\begin{aligned} [\bar{C}] = [C^o]([I] + c^i[\Gamma^i](c^i[I - S^i - \Gamma^i] + [S^i] + [A] \\ + c^v[I - S^v - \Gamma^v][S^v + B]^{-1}[S^i + A])^{-1} \\ + c^v[\Gamma^v](c^v(I - S^v - \Gamma^v] + [S^v] + [B] \\ + c^i[I - S^i - \Gamma^i][S^i + A]^{-1}[S^v + B])^{-1}) \end{aligned} \quad (8)$$

where brackets denote square matrices and $[A] = [C^i - C^o]^{-1}[C^o]$, $[B] = [C^v - C^o]^{-1}[C^o]$, c^r is the volume fraction of phase r, i identifies parameters relating to inclusions, and v identifies parameters relating to vacuoles.

The Eshelby tensor $[S]$ is dependent on the matrix Poisson's ratio, ν_o, and the inclusion shape. $[S]$ is defined [44] as

$$\begin{aligned} S_{ijkl} = \frac{1}{15(1 - \nu_o)}\{(5\nu_o - 1)\delta_{ij}\delta_{kl} \\ + (4 - 5\nu_o)(\delta_{ik}\delta_{jl} + \delta_{il}\delta_{jk})\} \end{aligned} \quad (9)$$

Vacuoles have been modelled as a spherical inclusion with orthotropic properties. For a uniaxial bar in

tension, a low modulus value, $F_b E_{11}$, in the loading or pole direction, was used to represent the debonded condition and a high or inclusion modulus value, E_{22} and E_{33}, in the equator direction was used together with setting $\nu_{12} = \nu_{21} = \nu_{13} = \nu_{31} = 0$ to enforce the lateral constraint condition. The factor F_b was introduced to allow for the possibility that a particle could be partially debonded. Because the M–T formulation can be applied equally well to inclusions with orthotropic properties as to inclusions with isotropic properties, this approach was implemented by modifying the definition of the debonded particle's material matrix. The property matrix for the normal components of this orthotropic material was

$$[C^v] = m\begin{bmatrix} F_b E_{11}(1-\nu_{23}\nu_{32}) & 0 & 0 \\ 0 & E_{22} & E_{22}\nu_{32} \\ 0 & E_{33}\nu_{23} & E_{33} \end{bmatrix} \quad (10)$$

where $m = (1 - \nu_{23}\nu_{32})^{-1}$, F_b is the partial debonding factor, E_{ii} the isotropic modulus of particle in the ii direction, and ν_{ij} the Poisson's ratio of particle in the ij direction.

The solution given [44] for particle interaction was integrated into the M–T formulation through a correction matrix, $[\Gamma^r]$. This matrix was derived from the analysis of probabilistic pairwise particle interaction of two identical and randomly located elastic spheres embedded in a comparison material. This was shown [42] to be

$$[\Gamma^r] = [I] + \frac{5c^r}{4\beta^2} Y [W^r] \quad (11)$$

where $[I]$ is the identity matrix, c^r the volume fraction of phase r, $Y = Y_m(1 - c^r)$, Y_m is the interaction factor multiplier, and $[W^r] = \zeta_1\delta_{ij}\delta_{kl} + \zeta_2(\delta_{ik}\delta_{jl} + \delta_{il}\delta_{jk})$. The definitions for β, ζ_1 and ζ_2 may be found elsewhere [44]. The term $[\Gamma^r]$ states that reinforcement not only comes from the presence of inclusions in the composite but that it also occurs due to the proximity of the inclusions to one another. The strength of the interaction is characterized by Y_m.

2.4. Non-linear elastic matrix behaviour

The average composite modulus $[\bar{C}]$ (Equation 8) is controlled by the nature of the constituent properties. If $[C^i]$ and $[C^o]$ are isotropic but $[C^v]$ is orthotropic, the average modulus will necessarily be orthotropic. If the $[C^i]$ and $[C^v]$ are linear elastic but $[C^o]$ is non-linear elastic, $[\bar{C}]$ will necessarily be non-linear elastic.

Non-linear elasticity has been introduced in the current micromechanical formulation by modelling the matrix as an isotropic strain-dependent material. This dependency was quantified by the second-order polynomial

$$E_o = a_0 + a_1\varepsilon_o + a_2\varepsilon_o^2 \quad (12)$$

where E_o is the tensile secant modulus of the matrix and ε_o is the average uniaxial matrix strain. The matrix Poisson's ratio, ν_o, was assumed to be constant over the strain range of interest. The E_o and ν_o were converted to strain-dependent bulk K_o and shear G_o secant moduli [46]. These were then used to calculate the elements in the matrix secant modulus $[C^o]$ according to standard relationships [47]. Because $[C^o]$ is defined in terms of a secant modulus, $[\bar{C}]$ is also a secant measure.

For a particulate composite containing an arbitrary number of phases, the average matrix strain was estimated using a Reuss model [48, 49]. The resulting relationship between ε_o and the average composite strain, ε_c, for a one-dimensional case was [50]

$$\varepsilon_o = \frac{E_c}{E_o}\varepsilon_c = M_\varepsilon \varepsilon_c \quad (13)$$

where E_c is the average composite secant modulus and M_ε is defined as the composite strain magnification factor. The fact that E_c, E_o and ε_c are functions of ε_o automatically means an iterative solution is required to solve Equation 8.

2.5. Prediction of mechanical behaviour

In order to predict the mechanical behaviour of a particulate composite using Equations 2–13, five things must be known before the critical strain, ε_{cr}, and the corresponding average composite stress, σ_c, can be calculated. They are:

1. the size distribution of the particles in the composite;
2. the particle and matrix properties;
3. the critical stress where particle debonding first begins;
4. the degradation in composite stiffness as a result of particles becoming debonded; and
5. the adhesion energy between particle and matrix.

Particle-size distribution and constituent properties can be measured using standard measurement techniques [41]. The technique to evaluate modulus degradation was discussed in Section 2.3. Estimation of adhesion energy will be dealt with in Section 3.3. Discussions on critical stress and further comments on adhesion energy are given in Section 4.1.2.

When the above items have been quantified, the prediction of composite mechanical behaviour proceeds in two steps. Up to the critical stress, σ_{cr}, before any debonding has occurred, the non-linear stress–strain relationship for a one-dimensional case maybe calculated according to

$$\varepsilon_c^{i+1} = (E_c^i)^{-1}\sigma_c^j \quad (14)$$

using the method of direct substitution [51]. Here, i is the iteration index, σ_c^j is the jth composite stress ($1 < j < M$, at $j = M$, $\sigma_c^M = \sigma_{cr}$), E_c^i is the average composite properties evaluated at ε_c^i and ε_c^{i+1} is the new estimate of ε_c.

After the critical stress has been reached, the solution continues with the debonding of the kth group of particles out of a total of K groups starting from the largest particle radius. Particle sizes in each group are calculated according to Equation 7. This determines

the energy dissipated through new surface area creation ($d\varepsilon_{area}$ in Equation 5) and the concentration of inclusions that have debonded. Calculation of the net change in average composite modulus (bracketed quantity on the right-hand side of Equation 4) is carried out using the modulus degradation routine from Section 2.3. From this, the critical strain is determined. The corresponding stress is then calculated using Equation 2 and the composite properties $[\bar{C}]$ which lead to the critical strain. Matrix strain is updated along with each critical strain calculated (Equation 13). As the process of debonding groups of inclusions carries on, the average mechanical behaviour of the composite is described by the pairs of critical strain–composite stress points.

3. Experimental procedure

3.1. Materials

A model composite material was fabricated using hydroxyl-terminated polybutadiene (HTPB) and spherical glass beads. The HTPB (Arco Chemicals) had a nominal molecular weight of 2800 g mol^{-1}, a polydispersity index of 1.8 and a hydroxyl equivalent weight of 40.2 mg KOH/g. Four types of glass beads were purchased from Potter's Industries Inc. (La Prairie, Qc, Canada) for the experiments. The first type was as-received beads with an advertised average diameter of 25 μm (Stock 2900). The second type was as-received beads with an advertised average diameter of 100 μm (Stock 2227). The third and fourth types were Stock 2900 and Stock 2227 treated with a silane coupling agent known as CP-03. This agent is optimized for use with epoxy and urethane resin systems.

The test matrix given in Table I was designed to examine the performance of the micromechanical model given different particle-size distributions, adhesion energies, inclusion volume fractions and loading rates. Each composite designation is composed of four letters. The first letter indicates the type of surface treatment (N, untreated; T, treated). The second letter indicates the initial inclusion volume fraction (3, 30%; 5, 50%). The third letter identifies the crosshead displacement rate used in the tensile test (M, 10 mm min^{-1}; F, 100 mm min^{-1}) and the fourth letter indicates the average bead size (S, 25 μm; L, 100 μm).

TABLE I Test matrix for glass bead/polybutadiene composites

Crosshead rate (mm min^{-1})	Treatment	Av. c_o^{i} [a] (%)	Av. diameter (μm)	Designation
10	None	30	25	N3MS
		30	100	N3ML
		50	25	N5MS
		50	100	N5ML
10	Silane	30	25	T3MS
		30	100	T3ML
		50	25	T5MS
		50	100	T5ML
100	None	30	25	N3FS
		30	100	N3FL
		50	25	N5FS
		50	100	N5FL
100	Silane	30	25	T3FS
		30	100	T3FL
		50	25	T5FS
		50	100	T5FL

[a] c_o^{i} is the initial inclusion volume fraction.

The model composite was fabricated in two steps. A pre-mix was prepared for casting by mixing in 0.5% wt/wt AO2246 (Cyanamid) anti-oxidant agent using a Design Integrated Technologies 10CV helicone vertical mixer. Mixing time was 2 h at 60 °C. The polymer was then left to stand under vacuum for 2 d at 60 °C to ensure that trace moisture had been eliminated. On the day of casting, 0.01% wt/wt di-terbutyl-dilaurate (DBTDL) cure catalyst from Aldrich Chemical was added to the pre-mix along with the required quantity of glass beads and mixed for 30 min. To achieve an optimal NCO/OH ratio of 1.1, 6.55% wt/wt tolylene diisocyanate (TDI, comprised of 97% 2,4 and 3% 2,6 isomers) from Kodak Ltd, was added and the entire mixture was mixed again for 30 min. At the end of the mix cycle, the composite was cast into 150 mm × 150 mm × 100 mm blocks for specimen preparation. All mixing and casting operations took place under vacuum. The blocks were left to cure for 6 d at 60 °C under ambient pressure.

3.2. Test procedures

Uniaxial specimens were prepared by sawing the composite blocks into 12.5 mm slabs and then die cutting JANNAF Class C type specimens from the slabs. The 9.5 mm × 12.5 mm cross-sectional area made this specimen well-suited for mechanical characterization of loaded materials [41, 52]. Prior to testing, the specimens were pre-conditioned in a vacuum desiccator at room temperature for at least 24 h.

Uniaxial testing was carried out on the composites in an Instron 4206 machine equipped with either an Optra Laser Extensometer (Optra Inc., Peabody, MA) or a Farris Gas Dilatometer (Richard Farris, Leeds, MA) according to CPIA procedures [52]. One series of tests were carried out with the laser extensometer to calculate the effective gauge length (EGL) of the model composites. Details of this procedure were given elsewhere [41]. Another series of tests were carried out in the gas dilatometer to measure simultaneously the stress–strain behaviour as well as the dilatation–strain behaviour. Details of how this instrument operates is given elsewhere [50, 53]. The EGL was needed for the dilatometer tests because composite strain could only be calculated using crosshead displacement. Three specimens were tested for each combination shown in Table I. Because data scatter was low, the test best representing the average behaviour of the three specimens was selected for use in Section 4. Tensile tests on pure polymer were conducted according to ASTM D638 [54].

Initial inclusion volume fraction, c_o^{i}, was measured using density measurements of pure polymer blocks and composite blocks. Density measurements were carried out using the immersion method as specified in ASTM D792-86 [55]. The initial volume fraction was

calculated using a rearrangement form of the rule of mixtures equation for composite density [45].

3.3. Estimation of adhesion energy

Adhesive strength has been measured using a number of techniques [56, 57]. As noted by Mower and Argon [58], these techniques evaluated the adhesive strength qualitatively through assumed adhesive characteristics or fractographic evidence. Mower and Argon [58] evaluated adhesive strength between particle and matrix in terms of a hydrostatic stress using a uniaxial test. Their test specimen consisted of a particle embedded in the centre of a matrix bar that was specially shaped to induce a triaxial state of stress at that point.

The approach used here was similar in concept to that used by Mower and Argon. However, instead of measuring adhesive strength, adhesion energy was desired. The basis of this measurement came from a simplified form of Equation 4 [42]

$$\frac{G_c}{V_o}\frac{\Delta A}{\Delta c_i} = -\frac{1}{2}\frac{\Delta E_c}{\Delta c_i}\varepsilon_{cr}^2 \quad (15)$$

Referring to Figs 1 and 2, Equation 15 states that if we load the specimen shown in Fig. 1 in tension, at some point ε_{cr}, there would be enough work input into the specimen to cause the glass bead to debond (point A in Fig. 2). When this occurs, there will be a sudden loss in reinforcement and therefore overall stiffness, so the load will fall to point B. If we unload from point B back to zero load (point O), the area OABO represents the energy dissipated to create new surface area. This energy is quantified by the right-hand term of Equation 15. Because the geometry of the specimen and inclusion are known and the amount of surface area debonded is observed during the test, adhesion energy, G_c, can be calculated.

The shape of the specimen shown in Fig. 1 was designed using a finite element model to concentrate the stress field around the pole of the glass bead and to minimize the peel stresses at the edges of specimen grips. The specimen volume was selected according to the size of beads available so that the $\Delta E_c/\Delta c_i$ would be measurable in terms of a drop in load at a reasonable crosshead displacement.

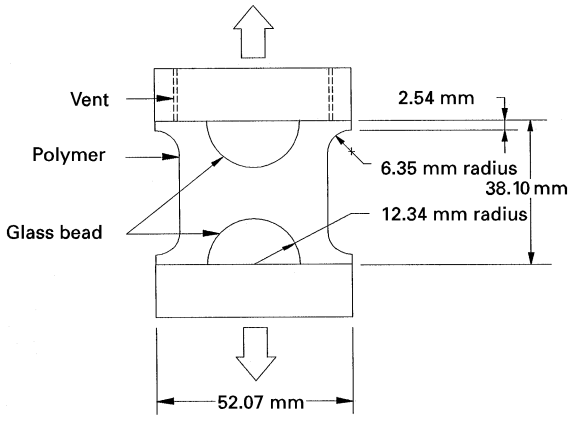

Figure 1 Geometry of test specimen used to measure adhesion energy.

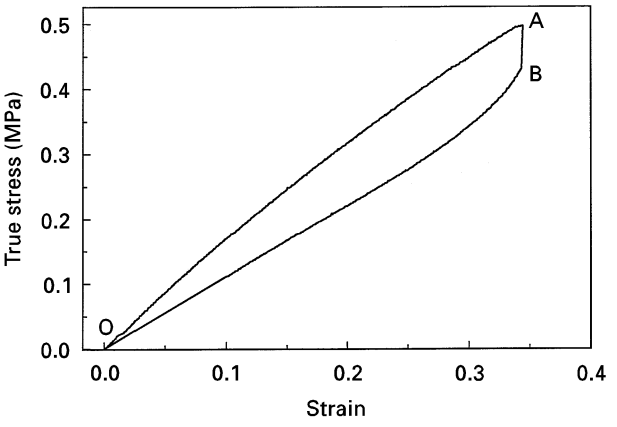

Figure 2 Schematic diagram of energy loss due to particle debonding.

Six specimens were fabricated using ordinary soda–lime beads (i.e. glass marbles) and HTPB polymer with an NCO/OH ratio of 1.0. The NCO/OH ratio was lowered slightly to match better the matrix modulus measured using specimens from the cast blocks in Section 3.1. The polymer modulus was verified using specimens that were fabricated without beads.

To fabricate the specimens, the beads and grip surfaces were degreased using dichloromethane. The lower grip was then set upright and the clamshell Teflon moulds, conforming to the geometry shown in Fig. 1, clamped on. The degassed polymer was poured into the mould while it was still at 60 °C. Afterwards, the top grip was pressed on and the excess polymer allowed to exit through the vents. This created essentially void-free specimens. Any air bubbles that did become trapped were usually small and located in the low stress areas in the specimen. These had negligible effect on the overall results.

The specimens were tested at two loading rates. Three specimens with beads and one specimen without beads were tested at a crosshead rate of $10\,mm\,min^{-1}$. The remaining specimens were tested at a rate of $100\,mm\,min^{-1}$. The purpose of these experiments was to obtain an idea of the relative change in adhesion energy for this type of composite at the two test speeds. No attempts were made to characterize the actual adhesion energy that existed between as-received glass beads or CP03-treated beads and HTPB. Therefore, the values estimated with these single-bead tests are not meant to be a representative measure of the adhesion energy present in the composites fabricated in Section 3.1 because the surface treatments are obviously different.

4. Analysis and discussion

The micromechanical model described in Section 2 contains adjustable parameters that must be defined before the model can be run. For example, the user must specify the appropriate value for the partial debonding factor, F_b (Equation 10). Questions of how one selects these values and how sensitive the predictions are to small changes in these values naturally arise.

The first question will be dealt with in Section 4.1. Here the experimental data will be used to deduce the values for the adjustable parameters. This analysis will also allow critical examination of the assumptions and theory presented in Section 2. The second question will then be examined in Section 4.2 in light of the parameters obtained in Section 4.1. In this section, because uniaxial tests were carried out, the notation used will refer to scalar values of tensile secant modulus, E, stress, σ, and strain, ε. Also, superscript "e" will be used to denote experimental data while superscript "c" will be used to denote calculated results. Comparisons will be made at discrete points so the differential operator has been replaced by a Δ operator to reflect this.

4.1. Determination of model parameters

4.1.1. Procedure

The known quantities in the model are the experimentally measured composite engineering stress, σ_c^{eng}, composite strain, ε_c^e, dilatation, $\Delta V^e/V$, initial inclusion fraction, c_o^i, particle distribution ($\bar{r}$ and n in Equation 7), isotropic matrix properties, E_o and ν_o, and isotropic particle properties, E_i and ν_i. The experimental true stress, σ_c^T, and secant modulus, E_c^e, can be calculated through the relationships [50]

$$\sigma_c^T = \sigma_c^{eng}\frac{1+\varepsilon_c^e}{1+\Delta V^e/V} \quad (16)$$

$$E_c^e = \sigma_c^T(\varepsilon_c^e)^{-1} \quad (17)$$

An example of the experimental data is shown in Fig. 3 for composite T3FS. As the composite is strained, no significant change in volume occurs until $\varepsilon_c \approx 0.12$. The stress corresponding to this strain was defined in Sections 2.3 and 2.5 as the critical stress, σ_{cr}. As strain increased, the cross-sectional area reduced according to the instantaneous composite Poisson's ratio. This resulted in the growing difference seen between composite true stress and engineering stress.

The unknown parameters in the model are the interaction factor multiplier, Y_m (Equation 11) and the partial debonding factor, F_b (Equation 10). Quantities such as the vacuole volume fraction, c_v (Equation 8) and the adhesion energy, G_c (Equation 4), even though not measured directly, can be deduced using the experimental data and the micromechanical model. Y_m can be determined using ε_c^e and E_c^e data up to σ_{cr}. After debonding occurs, ε_c^e, E_c^e and $\Delta V^e/V$ are needed to determine F_b and to deduce c_v.

The algorithm used to determine Y_m is shown in Fig. 4. The routine starts off by assuming $Y_m = 1$. It then proceeds by estimating the ith iteration of matrix strain, ε_o^i, using the jth pair of E_c^e–ε_c^e points in the data set. This value is used in the M–T routine (Equation 8) to calculate the E_c^c (Equation 3) that corresponds to ε_o^i. The same is done for E_o (Equation 12). A new value of ε_o^{i+1} is then calculated using E_c^c, E_o and ε_c^e (Equation 13). If the value of $\varepsilon_o^{i+1} \approx \varepsilon_o^i$, then the solution for the matrix strain has converged and the jth pair of calculated points, E_c^c–ε_c^e is stored. This continues for the M data points leading up to σ_{cr}. At $j = M$, the relative error between the experimental modulus, E_c^e, and calculated modulus, E_c^c, at each ε_c^e is calculated. If the average relative error, Y_m^{err}, between experimental and calculated moduli is greater than the tolerance, Y_m is adjusted and the entire procedure repeated. When $Y_m^{err} < \text{tol}$ then the appropriate interaction multiplier for the composite has been found.

The algorithm used to determine F_b is similar to that used for finding Y_m except this time, experimental values for modulus and dilatation are used (Fig. 5). The Y_m previously calculated is assumed to remain constant for the entire loading history. The routine starts off by assuming $F_b = 0$, i.e. the inclusion debonds completely with no residual stiffness in the loading direction. A quantity of vacuoles, c_v^j, are also assumed created as a result of debonding at the jth pair of E_c^e–ε_c^e and $\Delta V^e/V$–ε_c^e data points. As before, the solution for ε_o^i is allowed to converge. If $E_c^c \neq E_c^e$ then c_v^j is increased until this condition is met. The corresponding dilatation $\Delta V^c/V$ is calculated from

$$\frac{\Delta V^c}{V} = \left(1 - 2\frac{\bar{C}_{2211}}{\bar{C}_{2222}+\bar{C}_{2233}}\right)\varepsilon_c^e \quad (18)$$

The calculated pairs of $\Delta V^c/V$–ε_c^e are stored for $j = M+1$ to N where N is the total number of data

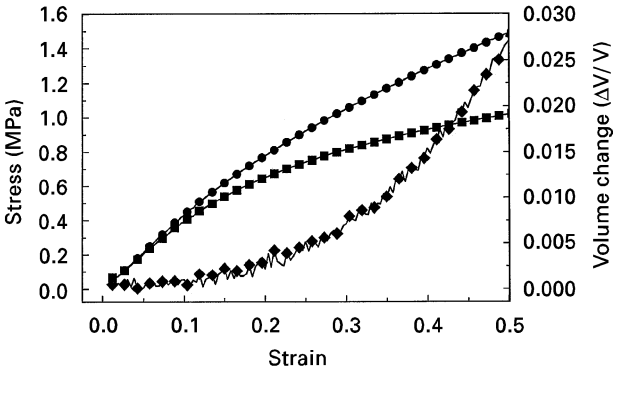

Figure 3 Experimental mechanical behaviour of composite T3FS. (■) Engineering stress, (●) true stress, (◆) dilatation.

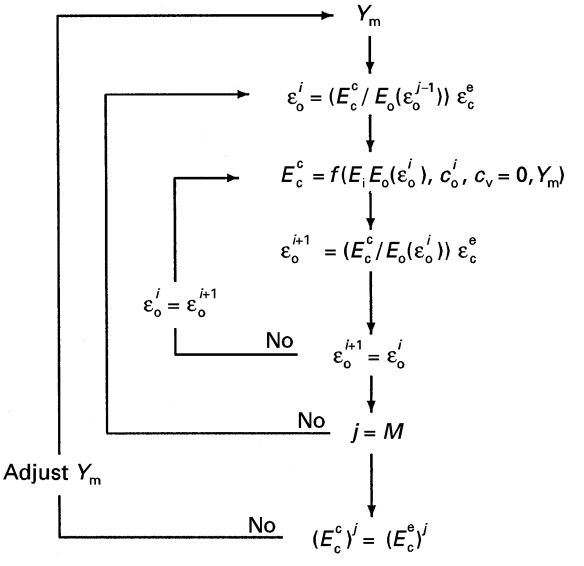

Figure 4 Algorithm for back calculation of Y_m.

points. At $j = N$, the average absolute error, F_b^{err}, between $\Delta V^c/V$ and $\Delta V^e/V$ is calculated. If the error is greater than the tolerance, then F_b is adjusted and the whole procedure repeated until the tolerance value is reached. When $F_b^{err} < \text{tol}$, the appropriate debonding factor for the composite has been found. Because a constant F_b is calculated, it represents the average degree of debonding for particles of all sizes in the composite.

An apparent adhesion energy, G_c^{app}, can be calculated from the experimental E_c^e–ε_c^e data and the parameterized particle distribution (Equation 7) by assuming that at the end of data, the total surface area debonded according to Equation 6 and Section 2.5 equals the total surface area debonded experimentally. In other words

$$\sum_{k=1}^{K} \Delta\varepsilon_{area}^{c} = \sum_{j=1}^{N} \Delta\varepsilon_{mod}^{e} \quad (19)$$

Rearrangement of Equation 19 in terms of Equation 15 gives,

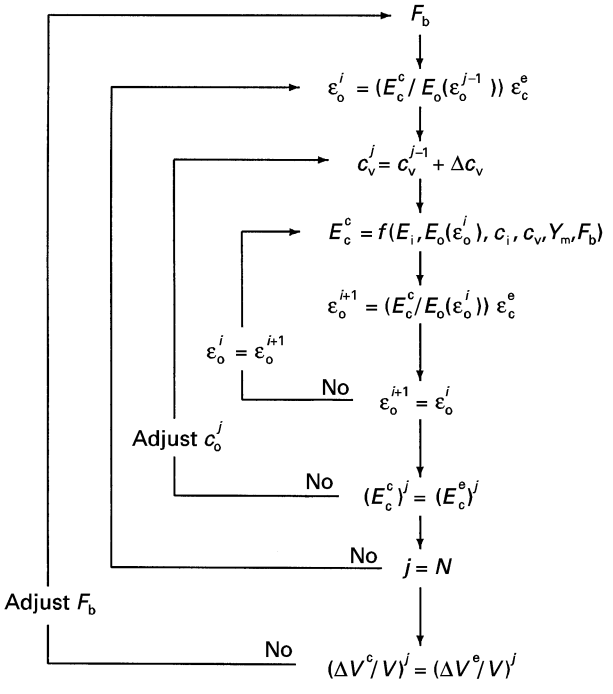

Figure 5 Algorithm for back calculation F_b.

$$G_c^{app} = \left(\frac{1}{2}\sum_{j=1}^{N}\frac{\Delta E_c^e}{\Delta c_i}\varepsilon_c^{e2}\right)\left(\frac{1}{V_o}\sum_{k=1}^{K}\frac{\Delta A}{\Delta c_i}\right)^{-1} \quad (20)$$

The summation of energy for $\Delta\varepsilon_{mod}^e$ is straight forward because it is simply the sum of all the energies dissipated at the N experimental data points. The summation for $\Delta\varepsilon_{area}^c$ is not as obvious because the total energy depends on the value selected for the total number of points, K, used to sub-divide the particle distribution. If K is large, the resulting sum of $\Delta A/\Delta c_i$ will be large because there will be many $1/r$ terms to add up. The opposite is true when K is small. The appropriate K was selected by matching the average Δc_i from the particle distribution with the average Δc_i deduced from the experimental data.

4.1.2. Results

The numerical results of the analyses described in Section 4.1.1 are shown in the lower part of Tables II and III. The upper part of the tables shows the measured model parameters. From the note included in the tables, it can be seen that the matrix modulus was slightly non-linear out to about 100%ε for the two crosshead rates used. The tolerances specified for Y_m^{err} ranged from 0.5%–5% while the tolerances for F_b^{err} ranged from 0.001–0.014. Different values were needed because the degree of fit between the experimental and calculated results were not always the same.

Figs 6–9 summarize the tensile and dilatational behaviour observed for the composites identified in the test matrix (Table I). Generally, the composites containing the CP-03 treated beads had higher maximum strength and lower dilatation than the equivalent composite which contained as-received beads. The treated beads also delayed the onset of dilatation. For the $c_o^i = 0.3$ composites, the initial modulus was unaffected by surface treatments or bead size. However, for the $c_o^i = 0.5$ composites, slight increases in initial moduli were seen for those composites containing as-received beads.

Figs 10–13 show the ability of the micromechanical model to reproduce the experimental data for composites T3FS–N3FS, T5FS–N5FS, T3ML–N3ML

TABLE II Model parameters for glass bead/HTPB tested at 100 mm min^{-1}

	T3FS	T3FL	T5FS	T5FL	N3FS	N3FL	N5FS	N5FL
$\bar{r}$(μm)	15.5	65	15.5	65	15.5	65	15.5	65
n	0.167	0.0374	0.167	0.0374	0.167	0.0374	0.167	0.0374
c_o^i	0.307	0.311	0.511	0.517	0.302	0.302	0.503	0.504
c_o^v	0.0	0.0	0.0	0.0	0.0	0.0	0.0	0.0
ν_i	0.16	0.16	0.16	0.16	0.16	0.16	0.16	0.16
ν_o	0.34	0.34	0.34	0.34	0.34	0.34	0.34	0.34
G_i(GPa)	30	30	30	30	30	30	30	30
E_o(MPa)	[a]	[a]	[a]	[a]	[a]	[a]	[a]	[a]
σ_{cr}(MPa)	0.5	0.5	0.9	0.95	0.35	0.30	0.65	0.8
Y_m	1.5	1.69	0.98	1.18	1.67	1.58	1.14	1.31
$F_b(\times 10^{-4})$	2.6	2.1	1.0	0.8	0.8	0.34	1.1	0.42
G_c^{app}(J m^{-2})	2.330	5.720	3.982	10.92	2.241	3.832	1.784	5.189

[a] $E_o = 1.522\,255 - 0.460\,286\varepsilon + 0.270\,235\varepsilon^2$ (MPa).

TABLE III Model parameters for glass bead/HTPB tested at 10 mm min^{-1}

	T3MS	T3ML	T5MS	T5ML	N3MS	N3ML	N5MS	N5ML
$\bar{r}$(μm)	15.5	65	15.5	65	15.5	65	15.5	65
n	0.167	0.0374	0.167	0.0374	0.167	0.0374	0.167	0.0374
c_o^i	0.307	0.311	0.511	0.517	0.302	0.302	0.503	0.504
c_o^v	0.0	0.0	0.0	0.0	0.0	0.0	0.0	0.0
ν_i	0.16	0.16	0.16	0.16	0.16	0.16	0.16	0.16
ν_o	0.34	0.34	0.34	0.34	0.34	0.34	0.34	0.34
G_i(GPa)	30	30	30	30	30	30	30	30
E_o(MPa)	[a]	[a]	[a]	[a]	[a]	[a]	[a]	[a]
σ_{cr}(MPa)	0.45	0.50	0.65	0.75	0.45	0.30	0.40	0.45
Y_m	1.17	1.26	0.83	1.13	1.22	0.92	1.06	1.32
$F_b(\times 10^{-4})$	2.1	1.8	1.0	1.1	0.4	0.24	1.0	0.3
G_c^{app}(J m^{-2})	1.204	3.651	2.229	6.344	1.428	2.218	1.134	2.908

[a] $E_o = 1.554\,865 - 0.497\,499\varepsilon + 0.321\,452\varepsilon^2$ (MPa).

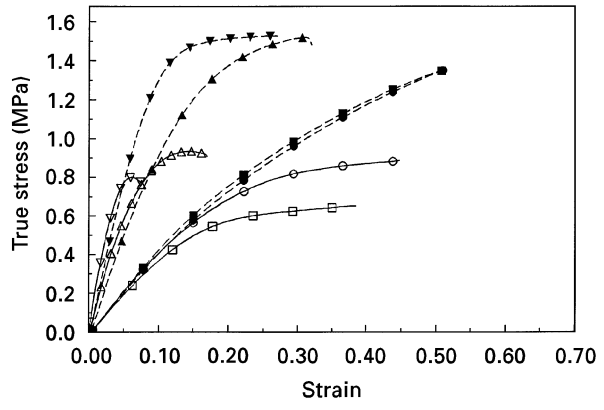

Figure 6 Experimental true stress results for (●, ▲, ■, ▼) treated and (○, △, □, ▽) untreated glass bead/HTPB composites tested at 10 mm min^{-1}. (○, ●, △, ▲) 32 μm, (□, ■, ▽, ▼) 120 μm; (○, □, ●, ■) 30%, (△, ▽, ▲, ▼) 50%.

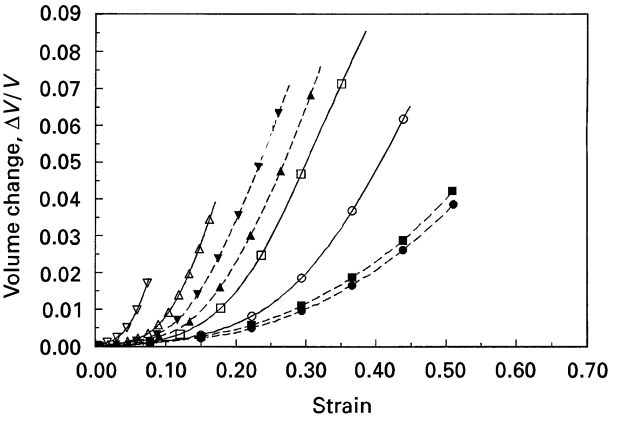

Figure 7 Experimental dilatation results for treated and untreated glass bead/HTPB composites tested at 10 mm min^{-1}. For key, see Fig. 6.

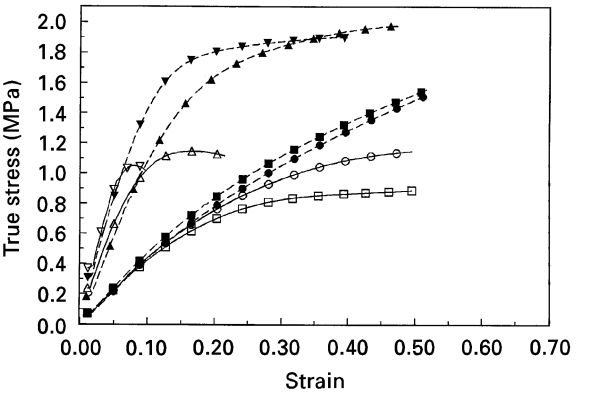

Figure 8 Experimental true stress results for treated and untreated glass bead/HTPB composites tested at 100 mm min^{-1}. For key, see Fig. 6.

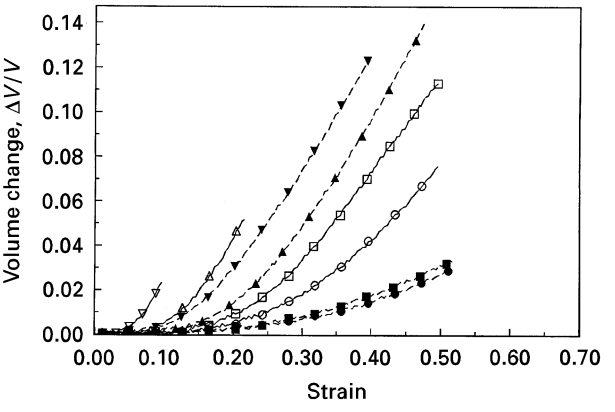

Figure 9 Experimental dilatation results for treated and untreated glass bead/HTPB composites tested at 100 mm min^{-1}. For key, see Fig. 6.

and T5MS–N5MS when the parameters from Tables II and III are used. For the sake of brevity, only the stress–dilatation–strain diagrams of these composites will be shown. For most composites including the ones not shown here, the calculated composite stress, σ_c^c, matches the experimental stress σ_c^e well up to the end of the data. It can be seen that the σ_c^c results have more of a "knee" when compared to the transition seen in the experimental data. The good fit between calculated results and experimental data indicate that the assumption of a constant Y_m was a reasonable one to make.

The deviations in calculated stress were closely related to the deviations of the calculated vacuole fraction, c_v^c, from the experimental vacuole fraction, c_v^e (Fig. 14). Because composite stresses are calculated from a current composite modulus that itself is dependent on the current vacuole fraction, it would be

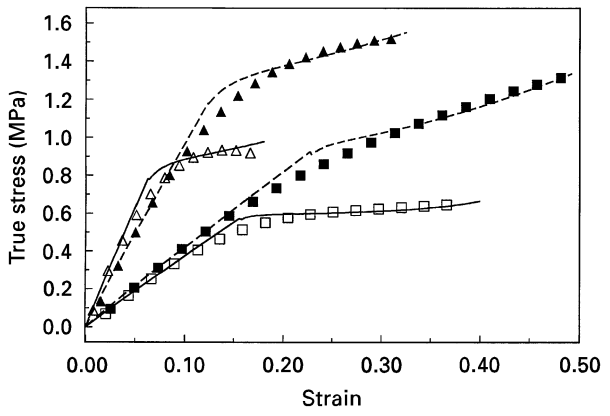

Figure 10 True stress behaviour calculations for selected (■, ▲, – – –) treated and (□, △, ——) untreated glass bead/HTPB composites tested at 10 mm min^{-1}. (■, □, ▲, △) Experimental results, (——, – – –) calculated results. (■, □) 30%, 120 μm, (▲, △) 50%, 32 μm.

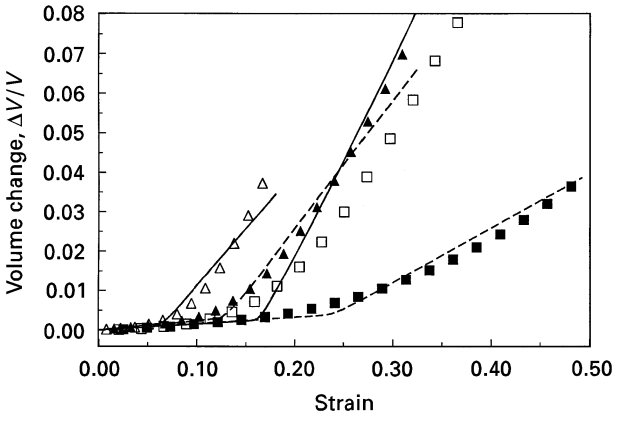

Figure 11 Dilatation behaviour calculations for selected treated and untreated glass bead/HTPB composites tested at 10 mm min^{-1}. For key, see Fig. 10.

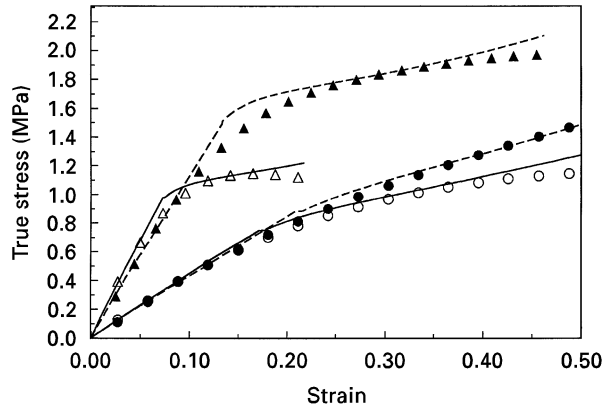

Figure 12 True stress behaviour calculations for selected (●, ▲, – – –) treated and (○, △, ——) untreated glass bead/HTPB composites tested at 100 mm min^{-1}. (○, ●, △, ▲) Experimental results, (——, – – –) calculated results. (○, ●) 30%, 32 μm, (△, ▲) 50%, 32 μm.

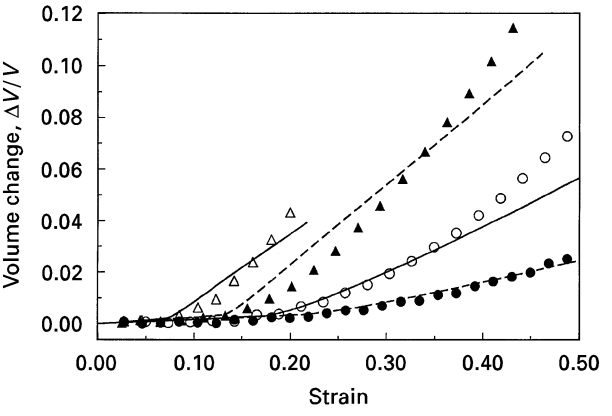

Figure 13 Dilatation behaviour calculations for selected treated and untreated glass bead/HTPB composites tested at 100 mm min^{-1}. For key, see Fig. 12.

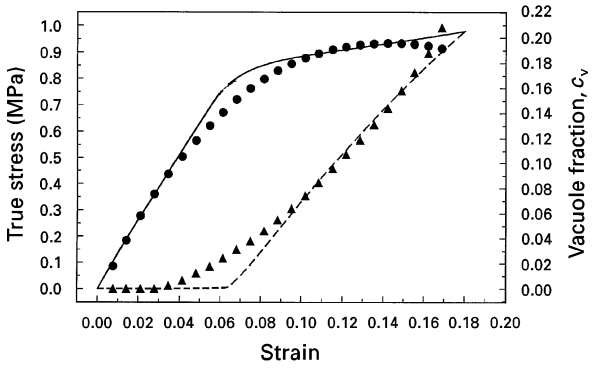

Figure 14 (●, —) True stress and (▲, – – –) vacuole concentration calculations for composite N5MS: (●, ▲) experimental, (——, – – –) calculated.

expected that the larger the deviation between calculated and experimental c_v, the larger the deviation between calculated and experimental σ_c. As foreseen, the σ_c^c to σ_c^e difference is opposite in sign and proportional to the c_v^c to c_v^e difference. The "knee" in the σ_c^c–ε_c^c curve is related to the apparent lack of strain energy available to debond the first set of particles. For example, in N5MS, debonding starts at $\varepsilon_c^e = 0.04$ in the experimental data as opposed to $\varepsilon_c^c = 0.06$ in the calculated results. The experimental results suggest that it may require less internal strain energy to initiate debonding than assumed in the micromechanical model. It should also be mentioned here that the requirement to specify σ_{cr} could be removed if a suitable initiation criterion could be found.

The calculated dilatational behaviour, $\Delta V^c/V$, tended to be on the stiff side when compared to the experimental dilatation, $\Delta V^e/V$. For cases such as T3FS and T5MS (Figs 11 and 13), the $\Delta V^c/V$ results compared well with the $\Delta V^e/V$ results. For other cases such as T5FS, N5FS and N5MS, $\Delta V^c/V$ was over estimated at the lower ε_c^e and under estimated at the higher ε_c^e. For N3ML, the $\Delta V^c/V$ was generally over estimated for the entire strain range, while for N3FS it was under estimated.

The $\Delta V^c/V$ results are controlled both by c_v and F_b. By assuming a value for F_b before determining the c_v that reproduces the E_c^e, the procedure described in Section 4.1.1 is only capable of finding an average debonding factor. In cases such as T3FS and T5MS, the assumption of a constant debonding factor appears to work well. In other cases such as T5FS, N5FS

or N5MS, it appears that the calculation of F_b needs to be refined in order to capture the debonding behaviour of the particles. Unfortunately, with only composite stress, strain and dilatation data on hand, there is not enough experimental information available to resolve this issue.

From Tables II and III, the result $Y_m \neq 1$ for all composites tested indicates that the composite modulus in Equation 8 requires some adjustment to reproduce the actual initial modulus. While it would be tempting to say that the Y_m values are purely attributable to physical particle interaction [59], the fact that the Y_m for composites containing $c_o^i = 0.5$ is lower than the Y_m for composites containing $c_o^i = 0.3$, except for the case of N3ML and N5ML, discounts this interpretation. From these results, Y_m can be considered a parameter that groups together factors such as particle interaction, size and surface treatment that have a subtle influence on composite modulus.

Again from the tables, it can be seen that the values of $F_b \neq 0$. This implies that the beads do not fully debond but that there is a residual bond that remains between bead and matrix. Physically, this would imply that $\theta \neq 0^\circ$ (Equation 6) as assumed by others [20, 60–62] but it would take on some value $\theta > 0^\circ$. This bond is significant because it varies between 1 and 12 times the stiffness of the matrix. The higher F_b for composites containing 31 μm beads suggests smaller beads debond to a lesser extent than larger beads.

One of the major assumptions made in the micromechanical model dealt with how particles debond as the composite is loaded. Based on the information found in the literature [22–25], it is generally accepted that large particles debond before smaller ones. This model takes that fact one step further by assuming that the particles in the composite debond in a progressive manner starting with the largest particles and ending with the smallest ones. The possibility that some large particles and some small particles debond at the same time is not considered. The experimental data and calculated results for rate of particle debonding (denoted Δc_v) versus the cumulative c_v for T5MS (Fig. 15) and N5MS (Fig. 16), show that the assumption was a reasonable one. This assumption worked well for 14 out of the 16 composites tested. In the cases of T5FL and T5ML, large differences were observed between the deduced Δc_v^e and the calculated Δc_v^c (see Fig. 17 for T5ML results). This explained why there was poor correspondence between the experimental and calculated σ_c–ε_c results (Fig. 18). Without other information, it is not possible to determine why the beads in these composites tended to debond at a slower rate than expected.

The apparent adhesion energies listed in Tables II and III indicate that the energy required to debond a particle is rate sensitive and must be taken into account. These values were calculated assuming the debonding angle $\theta = 0^\circ$. On average, when equivalent composites are compared, the G_c^{app} at 100 mm min^{-1} was about 1.7 times the G_c^{app} at 10 mm min^{-1}.

The results from the adhesion tests (Section 3.3) shown in Table IV also support this observation.

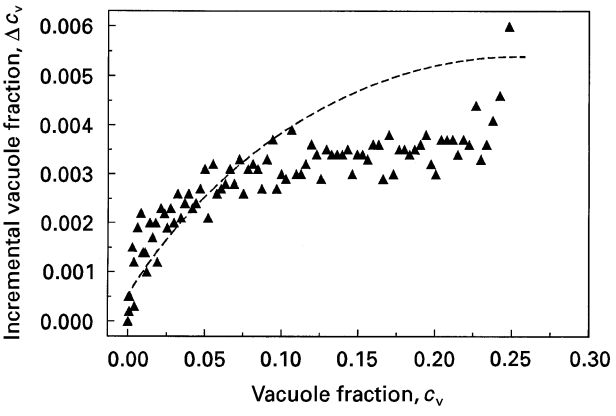

Figure 15 Calculated incremental vacuole concentration behaviour for composite T5MS. (▲) Experimental, (– – –) calculated values.

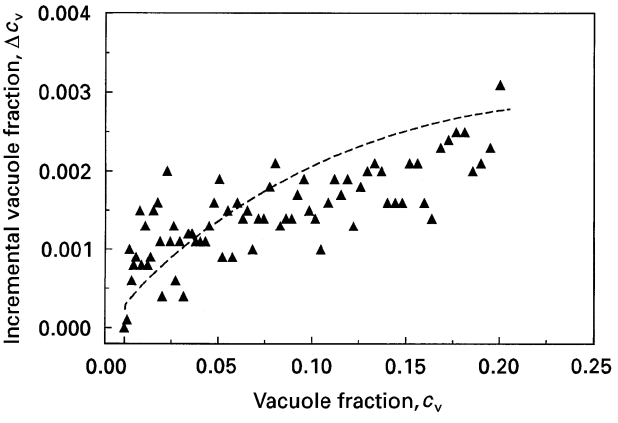

Figure 16 Calculated incremental vacuole fraction behaviour for composite N5MS. (▲) Experimental, (– – –) calculated values.

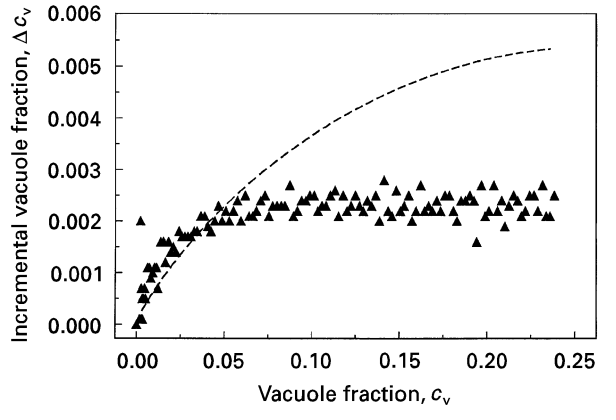

Figure 17 Calculated incremental vacuole concentration behaviour for composite T5ML. (▲) Experimental, (– – –) calculated values.

The average measured adhesion energy G_c^e at 10 mm min^{-1} was 374 J m^{-2}. At 100 mm min^{-1}, the average G_c^e was 758 J m^{-2}. Thus, the relative G_c^e magnitude based on the 10 mm min^{-1} result was 2.03. Fig. 19 compares the stress–strain data measured for Specimens 3 (10 mm min^{-1}) and 6(100 mm min^{-1}). It was interesting to note that the polymer failed around the bead at $\theta \approx 30^\circ$. This was predicted by the finite element results and has been predicted by others

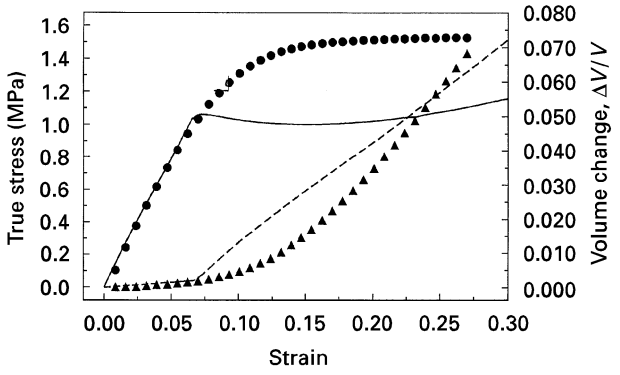

Figure 18 (●, ——) True stress and (▲, – – –) dilatation behaviour calculations for composite T5ML: (●, ▲) experimental, (——, – – –) calculated values.

TABLE IV Single bead debond results

Specimen	Rate (mm min^{-1})	E_c^{up}[a] (MPa)	E_c^{dn}[b] (MPa)	ε_{cr}	G_c^{app} (J m^{-2})
1	10	1.47	1.28	0.328	426
2	10	1.68	1.44	0.256	323
3	10	1.71	1.51	0.296	369
4	100	2.08	1.66	0.277	680
5[c]	100	N/A	N/A	N/A	N/A
6	100	1.85	1.52	0.350	835

[a] E_c^{up} is the average composite modulus when loading.
[b] E_c^{dn} is the average modulus when unloading.
[c] Results for Specimen 5 are not available because it failed prematurely.

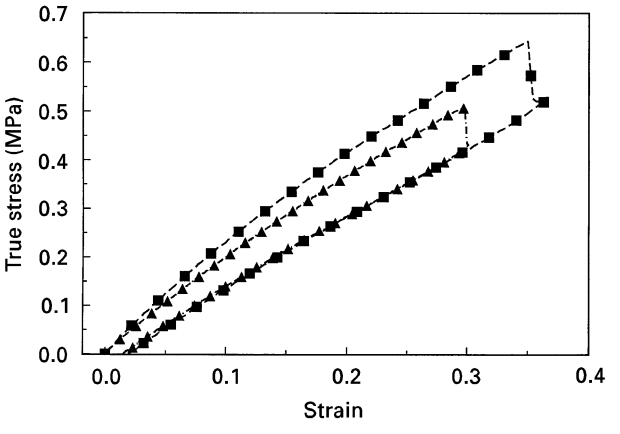

Figure 19 Adhesive energy dissipation for debond specimens tested at (▲) 10 and (■) 100 mm min^{-1}.

[63, 64]. If the particles in the model composites debonded in a similar manner then this would mean the results in Tables II and III are under estimated by a factor of 2.

It is difficult to pin-point what the actual G_c is for the different beads used. In general, the treated beads had larger G_c^{app} than the untreated beads. Exceptions to this were the composites containing 30% volume fraction of the 31 μm beads. Comparisons of $\Delta V^e/V$ versus ε_c^e show that the as-received beads debonded earlier than the treated beads in all cases (Figs 9 and 11). This result demonstrates clearly that the bonding for treated beads was better because more strain energy was required in the composite to induce debonding. The tables, however, also suggest that the 130 μm beads have a larger G_c than that 31 μm beads and that G_c increases with increases in c_o^i. There are no obvious reasons why this should be so. The fact that the model can reproduce the $\sigma_c^e - \varepsilon_c^e$ and $\Delta V^e/V - \varepsilon_c^e$ behaviour using G_c^{app} suggests there was validity in assuming equal amounts of surface area have been debonded in the actual and model particle distributions. At this point, the values for G_c can only be called "apparent" because the factors that influence this parameter have yet to be precisely determined. This remains a problematic area for this model. Quantification of energy dissipation by mechanisms other than surface creation in composites has been studied [65–67] though, and may lead the way for further work.

4.2. Sensitivity and predictive capability of micro-mechanical model

The back-calculated parameters found in the previous section reduced the error in modulus and dilatation to a minimum. The sensitivity of the micromechanical model to changes in the adjustable parameters will be examined from two perspectives. The first is to examine the tendencies the model exhibits with changes in the parameters. This will identify the dominant parameter. The second is to use the model like a user would to predict the mechanical behaviour of a composite under development. This will demonstrate the predictive capability of the model given the presence of the adjustable parameters.

Four parameters, namely σ_{cr}, Y_m, F_b and G_c were needed in the model. Out of these four, only Y_m and F_b can be considered truly adjustable. σ_{cr} was specified by examining the measured stress–strain and dilatation–strain results (Section 4.1.1). G_c is a measurable quantity too, although it is not clear how it should be measured. As a consequence, the sensitivity analyses presented in the following sections will use σ_{cr} and G_c^{app} as shown in Tables II and III. Y_m and F_b will be varied. Analyses are limited to the 10 mm min^{-1} parameters because the 100 mm min^{-1} parameters have the same trends based on composite type.

4.2.1. Trends with Y_m and F_b

To make the analysis manageable, the sensitivity of a single point on the σ_c^e–ε_c^e and $\Delta V^e/V$–ε_c^e curves were selected for comparison with the calculated values. These points were called target values and were generally chosen at the mid-way point in the phase where particles were debonding because they would measure the average change in behaviour. Table V lists this information along with the corresponding target Y_m and F_b (see also Figs 10 and 11). The term "fractional value" will be used often. This is defined by

$$\text{fraction} = \frac{\text{actual}}{\text{target}} - 1 \qquad (21)$$

The fractional stress and dilatation values were calculated over a fractional Y_m and F_b of ± 0.25 in steps

of 0.05. This produced 100 different combinations to examine for each composite. For the sake of brevity, only the graphical results of T5MS and N5MS will be shown. The composites T3ML and N3ML exhibited similar behaviour.

A comparison of the fractional stress contours for T5MS (Fig. 20) and N5MS (Fig. 22) shows that the stress sensitivities are quite different. In T5MS, there are high rates of change centred at fractional $Y_m = -0.20$ and $F_b = 0.15$. In N5MS, the gradient is more uniform. A similar pattern is observed in the dilatational sensitivities (Figs 21 and 23). In all the figures, high fractional stresses or low fractional dilatations are seen when fractional F_b is high and Y_m is low. Because a high fractional F_b increases stiffness, one would expect high stresses there. However, a high fractional Y_m, also increases stiffness but low stresses tend to occur in those locations. This shows that the model is influenced more by the value of F_b than Y_m. The figures reveal that it is better to under estimate F_b and over estimate Y_m if reasonably accurate values of stress (fractional $\sigma_c < 10\%$) are desired. This would be to the detriment of the dilatation results though. Table VI summarizes the locations of the minimum and maximum fractional stresses and dilatations for all composites examined in this section.

For interest, a similar analysis was carried out for fractional values of σ_{cr} and G_c^{app} while Y_m and F_b were fixed according to Tables II and III. Figs 24 and 25 show that stress and dilatation are totally dominated by G_c^{app}. For the range studied ($-0.15 <$ frac.$G_c^{app} < +0.15$), the stresses are within 10% of the target values. Dilatation is only slightly affected by changes in G_c^{app} in comparison to the effects of F_b. The analysis was limited to ± 0.15 because greater values

TABLE V Target values for sensitivity analyses

Composite	ε_c^e	σ_c^e (MPa)	$\Delta V^e/V$	Y_m	F_b ($\times 10^{-4}$)
T3ML	0.400	1.19	0.023	1.26	1.8
N3ML	0.301	0.626	0.050	0.92	0.24
T5MS	0.249	1.46	0.042	0.83	1.0
N5MS	0.150	0.933	0.028	1.06	1.0

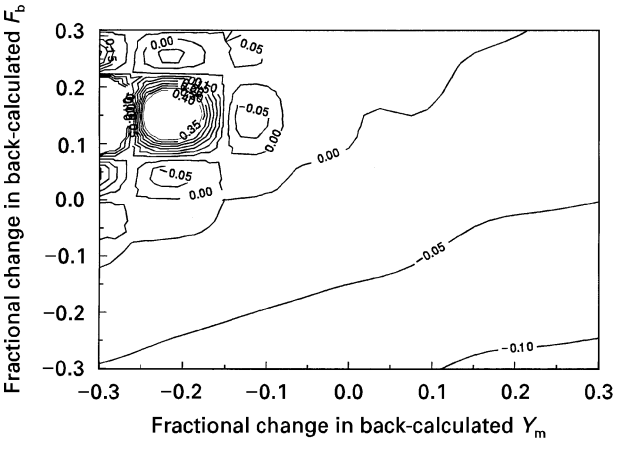

Figure 20 Fractional stress contours for composite T5MS based on variation of interaction factor, Y_m and debonding factor, F_b.

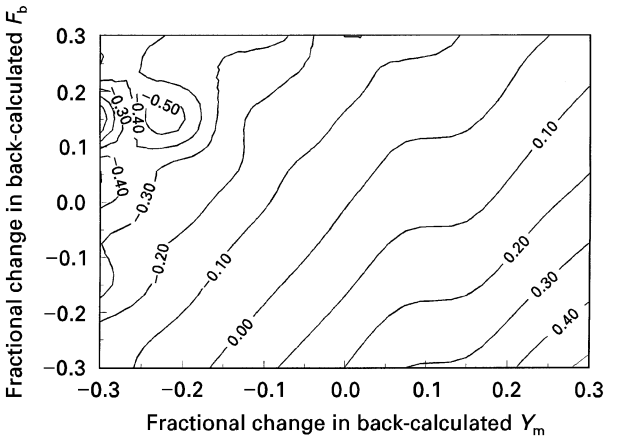

Figure 21 Fractional dilatation contours for composite T5MS based on variation of interaction factor, Y_m and debonding factor, F_b.

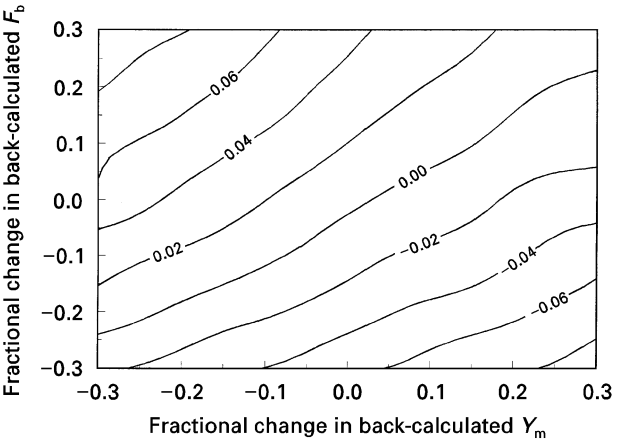

Figure 22 Fractional stress contours for composite N5MS based on variation of interaction factor, Y_m and debonding factor, F_b.

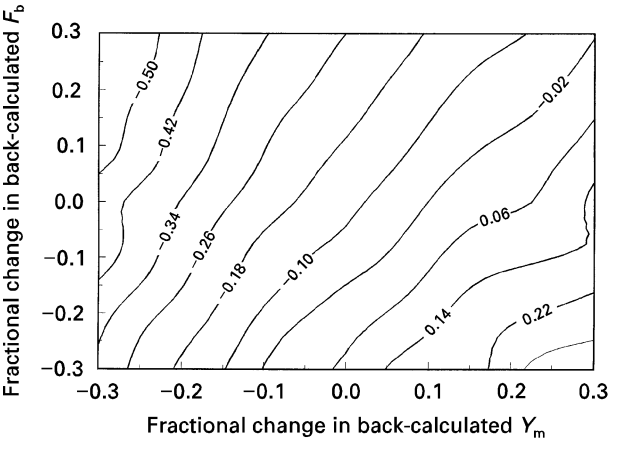

Figure 23 Fractional dilatation contours for composite N5MS based on variation of interaction factor, Y_m and debonding factor, F_b.

caused large increases in fractional stress. The results' insensitivity to variations in σ_{cr} highlight again the importance of having a representative value for G_c.

4.2.2. Predictive capability of model

To use the micromechanical model for predicting mechanical behaviour of an unknown composite, a set

TABLE VI Minimum and maximum fractional, σ_c and $\Delta V/V$

Composite		Fractional					
		σ_c	F_b	Y_m	$\Delta V/V$	F_b	Y_m
T3ML	Max	0.02	0.25	− 0.25	0.50	− 0.25	0.20
	Min	− 0.08	− 0.25	0.25	− 0.30	0.25	− 0.25
N3ML	Max	0.06	0.25	− 0.25	0.65	− 0.25	0.20
	Min	− 0.10	− 0.25	0.25	0.05	0.25	− 0.25
T5MS	Max	0.40	0.15	− 0.20	0.40	− 0.25	0.25
	Min	− 0.10	− 0.25	0.25	− 0.50	0.15	− 0.20
N5MS	Max	0.08	0.25	− 0.25	0.30	− 0.25	0.25
	Min	− 0.08	− 0.25	0.25	− 0.50	0.25	− 0.25

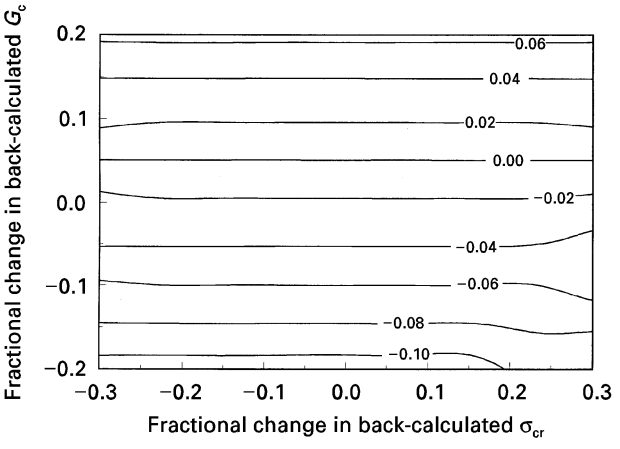

Figure 24 Fractional stress contours for composite T5MS based on variation of critical stress, σ_{cr}, and apparent adhesion energy, G_c^{app}.

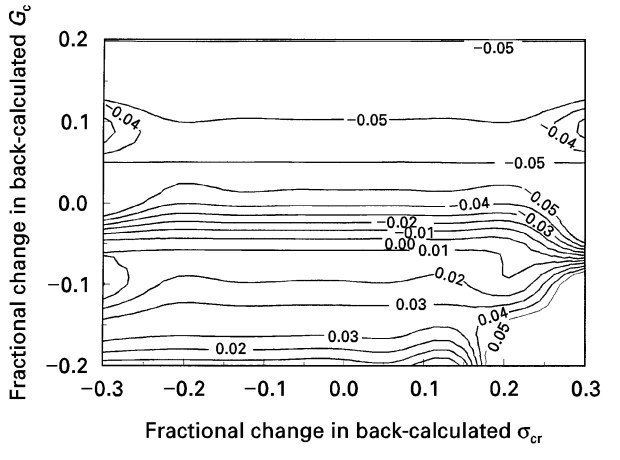

Figure 25 Fractional dilatation contours for composite T5MS based on variation of critical stress, σ_{cr}, and apparent adhesion energy, G_c^{app}.

of "best guess" Y_m and F_b values are required. It is evident from Table III that the F_b for treated particles is not in the same range as the F_b for as-received particles. As it was determined in the previous section that it was better to under estimate F_b, a "best guess" value of $F_b = 1.0 \times 10^{-4}$ was selected for the treated particles and a value of 0.25×10^{-4} was selected for the as-received ones. A reasonable "best guess" value of $Y_m = 1.0$ was selected because the model is less sensitive to variations in Y_m and it was a nice round number.

TABLE VII Fractional σ_c and $\Delta V/V$ for best guess Y_m and F_b

Composite	Best guess		Fractional			
	Y_m	F_b	Y_m	F_b	σ_c	$\Delta V/V$
T3ML	1.0	1.00×10^{-4}	− 0.21	− 0.44	≈ −0.08	≈ +0.50
N3ML	1.0	0.25×10^{-4}	+ 0.09	+ 0.04	≈ −0.02	≈ +0.30
T5MS	1.0	1.00×10^{-4}	+ 0.20	+ 0.00	≈ −0.05	≈ +0.10
N5MS	1.0	0.25×10^{-4}	− 0.06	− 3.00	−0.22	+0.74

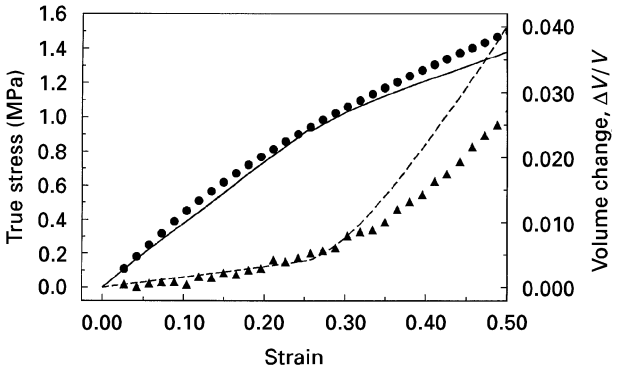

Figure 26 Predicted mechanical behaviour of composite T3FS based on best-guess parameters derived from 10 mm min^{-1} results. (●) Experimental stress, (▲) experimental dilatation, (——) calculated stress, (– – –) calculated dilatation.

The results of using these "best guess" values are shown in Table VII. For T3ML, N3ML and T5MS, the fractional stresses are less than 0.1 as expected. Composite N5MS fell outside this range because, unlike the other untreated composites, its back-calculated F_b was closer to 1.0×10^{-4}. The N5MS values were calculated by hand because they were well beyond the limits of Figs 22 and 23. The fractional dilatation were high, as expected.

As a final evaluation of these "best guess" values, they were used to predict the behaviour of composites T3FS and N3FS. From Fig. 26, it can be seen that σ_c^c for T3FS compares well with σ_c^e. It is slightly lower than the σ_c^c calculated with back-calculated values (Fig. 12). The $\Delta V^c/V$ is over estimated in relation to $\Delta V^e/V$ and the $\Delta V^c/V$ calculated with optimal values (Fig. 13). For N3FS, the trends are similar except the difference between σ_c^c and σ_c^e is more noticeable (Figs 27 and 12). This shows that it is possible to

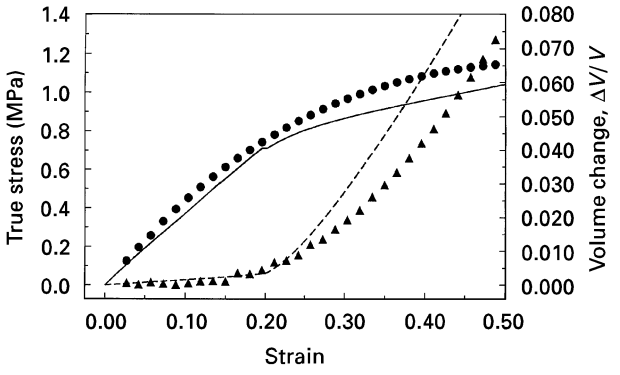

Figure 27 Predicted mechanical behaviour for composite N3FS based on best-guess parameters derived from 10 mm min^{-1} results. For key, see Fig. 26.

predict the mechanical behaviour of particulate composites if suitable values for σ_{cr} and G_c^{app} are available.

5. Conclusion

A micromechanical model for analysis of particulate mechanical behaviour has been presented. The following assumptions were used during the model development.

1. Non-linear effects are due to matrix and particle debonding.
2. Only well-bonded particles, debonded particles and matrix are present in the composite.
3. Well-bonded particles are characterized by isotropic properties while debonded particles are approximated with orthotropic properties.
4. The matrix is non-linear elastic.
5. The representative volume element is much larger than the largest particle.
6. The interaction multiplier and debonding factor are constant throughout the loading history.
7. Particles debond progressively from largest sizes to smallest sizes throughout the strain history.

The study was broken into two sections. The first section used the experimental data from a range of glass bead/HTPB composites to back-calculate model parameters. Reasonable values for the parameters were found. This showed that the micromechanical model gave a good representation of the processes believed to control mechanical behaviour. The deviations between calculated and experimental stress were small when the back-calculated parameters were used. Larger deviations for dilatation existed. These deviations were traced back to differences between the calculated and deduced vacuole volume fractions.

A comparison between the back-calculated interaction multipliers for the different composites showed that composite modulus is not only a function of volume fraction and particle interaction but it may be influenced by particle size and surface treatment as well. The non-zero debonding factors found in this study suggested that particles cannot be assumed to debond fully. Assumption 7 was confirmed indirectly by using the incremental vacuole fraction as an indicator of the particle sizes debonded at any given moment.

The second section examined the sensitivity of the model results to small changes in the interaction multiplier and debonding factor. The debonding factor was found to have a dominating effect on the calculated results. Changes in composite stress were less sensitive to changes in this factor than composite dilatation. The results showed it was better to under estimate the debonding factor and to over estimate the interaction multiplier when modelling an unknown composite. An additional analysis showed that the apparent adhesion energy also dominated the model results. The model's dependency on representative adhesion characteristics remains a problematic area due to the difficulty in measuring such values.

Based on the sensitivity results, "best guess" interaction and debonding parameters were selected to examine the predictive capability of the model. The critical stress and adhesion energy were assumed known. In most cases, the predicted composite stresses were within 10% of the experimental data. Dilatation was usually over-predicted. As an additional test, the behaviour for two composites tested at 100 mm min^{-1} were predicted using the "best guess" 10 mm min^{-1} interaction multiplier and debonding factor. The results showed that the model was capable of predicting the mechanical behaviour as long as suitable values for critical stress and adhesion energy were available.

Acknowledgements

The authors thank the Defence Research Establishment Valcartier management for their support in this work. The assistance given by Mr P. Carignan and Mr M. Kervarec, DREV, during the fabrication of the debond specimens is greatly appreciated. The work carried out by Mr R. Coulombe and Mr L. Bourret, DREV, to fabricate the glass bead/HTPB composites is also acknowledged. The helpful discussions with Dr C. Dubois, DREV, are also appreciated.

References

1. A. M. FREUDENTHAL and M. SHINOZUKA, *AIAA J.* **1** (1963) 107.
2. L. R. HERRMANN, *ibid.* **3** (1965) 1896.
3. R. A. SCHAPERY, in "Proceedings of the ICRPG/AIAA 3rd Solid Propulsion Conference", Atlantic City, 4–6 June 1968 (AIAA, Reston, VA) Paper 68-520.
4. R. J. FARRIS, "Development of a Solid Rocket Propellant Nonlinear Constitutive Theory", Phillips Laboratory, Report AFRPL-TR-75-20 (1975).
5. T. Y. LEE, *AIAA J.* **17** (1979) 1015.
6. T. L. COST, in "Proceedings of the AIAA/SAE/ASME 18th Conference", Cleveland, 21–24 June 1982 (AIAA, Reston, VA) Paper 82-1098.
7. S. R. SWANSON and L. W. CHRISTENSEN, *J. Spacecraft* **20** (1983) 559.
8. I. W. JONES and E. PIERRE-LOUIS, *Computers Structures* **21** (1985) 235.
9. C. P. BUCKLEY, *Rheol. Acta* **27** (1988) 224.
10. M. BURKE, P. WOYTOWITZ and G. REGGI, *J. Propulsion Power* **8** (1992) 586.
11. S. OZUPEK and E. B. BECKER, *J. Engng Mater. Technol.* **114** (1992) 111.
12. F. R. SCHWARZL, "Mechanical Properties of Highly Filled Polymers III", Central Laboratory TNO Delft (Netherlands), Report CL-64/49 (1964).

13. R. A. SCHAPERY, "A Nonlinear Constitutive Theory for Particulate Composites Based on Viscoelastic Fracture Mechanics", Texas A and M, Report MM2764-73-1 (1973).
14. A. H. LEPIE and A. ADICOFF, *J. Appl. Polym. Sci.* **19** (1975) 2821.
15. R. A. SHAPERY, *Engng Fract. Mech.* **25** (1986) 845.
16. B. J. SULLIVAN and Z. HASHIN, "Analysis of the Properties of Solid Propellants", Materials Sciences Corporation, Report MSC/TFR/1901/8305 (1988).
17. I. L. DAVIS and R. G. CARTER, "Microstructural Propellant Constitutive Theory", Vol. 1, Astronautics Laboratory, Report AL-TR-89-009 (1989).
18. T. L. SMITH, *Trans. Soc. Rheol.* **3** (1959) 113.
19. R. J. FARRIS, *ibid.* **12** (1968) 315.
20. L. L. VRATSANOS-ANDERSON and R. J. FARRIS, *Polym. Engng Sci.* **33** (1993) 1458.
21. *Idem*, *ibid.* **33** (1993) 1466.
22. J. LEIDNER and R. T. WOODHAMS, *J. Appl. Polym. Sci.* **18** (1974) 1639.
23. M. MORTON, R. J. MURPHY and T. C. CHENG, *Adv. Chem. Series* **142** (1974) 409.
24. G. LANDON, G. LEWIS and J. F. BODEN, *J. Mater. Sci.* **12** (1977) 1605.
25. D. W. NICHOLSON, *J. Adhesion* **10** (1979) 255.
26. J. C. SMITH, G. A. KERMISH and C. A. FENSTERMAKER, *ibid.* **4** (1972) 109.
27. P. DREYFUSS, A. N. GENT and J. R. WILLIAMS, *J. Polym. Sci. Polym. Phys. Ed.* **18** (1980) 2135.
28. B. PUKANSZKY, *Composites* **21** (1990) 255.
29. J. A. KING, D. A. BUTTRY and D. F. ADAMS, *Polym. Compos.* **14** (1993) 292.
30. M. SUMITA, T. OOKUMA, K. MIYASAKA and K. ISHIKAWA, *J. Appl. Polym. Sci.* **27** (1982) 3059.
31. S. N. MAITI and P. K. MAHAPATRO, *ibid.* **42** (1991) 3101.
32. J. C. HALPIN and J. L. KARDOS, *Polym. Engng Sci.* **16** (1976) 344.
33. R. F. FEDORS, *Polymer* **20** (1979) 324.
34. Z. HASHIN and S. SHTRIKMAN, *J. Mech. Phys. Solids* **11** (1963) 127.
35. L. J. WALPOLE, *ibid.* **17** (1969) 235.
36. Z. HASHIN, *ibid.* **40** (1992) 767.
37. N. LAWS and R. McLAUGHLIN, *Proc. R. Soc. Lond. Ser. A* **359** (1978) 251.
38. F. LENE and D. LEGUILLON, *Int. J. Solids. Struct.* **18** (1982) 443.
39. A. NEEDLEMAN, *J. Appl. Mech.* **54** (1987) 525.
40. Y. P. QIU and G. J. WENG, *ibid.* **59** (1992) 261.
41. F. C. WONG and A. AIT-KADI, *J. Appl. Polym. Sci.* **55** (1995) 263.
42. *Idem*, *J. Compos. Mater.* **31** (1997) 104.
43. T. MORI and K. TANAKA, *Acta Metall.* **21** (1973) 571.
44. J. W. JU and T. M. CHEN, *Acta Mech.* **103** (1994) 123.
45. F. C. WONG, "Mechanical Behaviour of Particulate Composites: Experiments and Micromechanical Predictions", Defence Research Establishment Valcartier, Report R-9403/94 (1994).
46. O. HOFFMAN and G. SACHS, "Introduction to the Theory of Plasticity for Engineers" (McGraw-Hill, New York, 1953).
47. G. E. MASE and G. T. MASE, "Continuum Mechanics for Engineers" (CRC Press, Boca Raton, FL, 1991).
48. R. L. McCULLOUGH, in "Delaware Composites Design Encyclopedia", Vol. 2 edited by L. A. Carlsson and J. W. Gillespie, Jr. (Technomic, Lancaster, 1990) pp. 93–142.
49. J. G. BENNETT and K. S. HABERMAN, *J. Compos. Mater.* **30** (1996) 1732.
50. U. YILMAZER and R. J. FARRIS, *J. Appl. Polym. Sci.* **28** (1983) 3369.
51. R. D. COOK, D. S. MALKUS and M. E. PLESHA, "Concepts and Applications of Finite Element Analysis" (Wiley, New York, 1989) pp. 502–4.
52. J. E. FITZGERALD and W. L. HUFFERD (eds) "Uniaxial Tensile Tests at Constant Strain Rate" in "Solid Propellant Mechanical Behaviour Manual", Publ. 21 (Chemical Propulsion Information Agency, Silver Spring, 1970) p. 4.3.2-1.
53. L. L. ANDERSON, PhD dissertation, University of Massachusetts (1989).
54. R. A. PRIEMON-STORER (ed.) Test Method for Tensile Properties of Plastics, ASTM D638-82a (American Society for Testing and Materials, Philadelphia, PA, 1984).
55. Density and Specific Gravity (Relative Density) of Plastics by Displacement, ASTM D792-86 (American Society for Testing and Materials, Philadelphia, PA, 1987).
56. G. R. HAMED, *Rubber Chem. Tech.* **64** (1991) 493.
57. P. HERRERA-FRANCO and L. T. DRZAL, *Composites* **23** (1992) 2.
58. T. M. MOWER and A. S. ARGON, *J. Mater. Sci.* **31** (1996) 1585.
59. R. K. EVERETT, *J. Compos. Mater.* **30** (1996) 748.
60. T. MOCHIDA, T. MINORU and M. OBATA, *JSME Int. J. Series I* **34** (1991) 187.
61. W. TONG and G. RAVICHANDRAN, *Compos. Sci. Technol.* **52** (1994) 247.
62. S. BAZHENOV, *Polym. Engng Sci.* **35** (1995) 813.
63. G. P. TANDON and G. J. WENG, *J. Appl. Mech.* **53** (1986) 511.
64. S. MITSUI, H. KIHARA, S. YOSHIMI and Y. OKAMOTO, *Polym. Engng Sci.* **36** (1996) 2241.
65. K. FRIEDREICH and U. A. KARSH, *J. Mater Sci.* **16** (1981) 2167.
66. A. NEEDLEMAN, *Ultramicroscopy* **40** (1992) 203.
67. Y. HUANG, D. L. HUNSTON, A. J. KINLOCH and C. K. RIEW, *Adv. Chem. Ser.* **233** (1993) 1.

Received 2 January
and accepted 25 March 1997